Modelling urban floods using a finite element staggered scheme with an anisotropic dual porosity model.

Daniele P. Viero[a]

[a]*Department ICEA, University of Padova, Via Loredan 20, 35131 Padova, Italy.*

Abstract

In porosity models for urban flooding, artificial porosity is used as a statistical descriptor of the urban medium. Buildings are treated as subgrid-scale features and, even with the use of relatively coarse grids, their effects on the flow are accounted for. Porosity models are attractive for large-scale applications due to limited computational demand with respect to solving the classical Shallow Water Equations on high-resolution grids. In the last decade, effective schemes have been developed that allowed accounting for a wealth of sub-grid processes; unfortunately, they are known to suffer from oversensitivity to mesh design in the case of anisotropic porosity fields, which are typical of urban layouts. In the present study, a dual porosity approach is implemented into a two-dimensional Finite Element numerical scheme that uses a staggered unstructured mesh. The presence of buildings is modelled using an isotropic porosity in the continuity equation, to account for the reduced water storage, and a tensor formulation for conveyance porosity in the momentum equations, to account for anisotropy and effective flow velocity. The element-by-element definition of porosities, and the use of a staggered grid in which triangular cells convey fluxes and continuity is balanced at grid nodes, allow avoiding undesired mesh-dependency. Tested against refined numerical solutions and data from a laboratory experiment, the model provided satisfactory results. Model limitations are discussed in view of applications to more complex, real urban layouts.

Keywords: Urban flooding, Anisotropic porosity model, Shallow flow, Large-scale inundation models, Mesh independence, Subgrid model

1. Introduction

Floods are undoubtedly a major threat of our time (Blöschl et al., 2017; Doocy et al., 2013); of all the victims of annual natural disasters, more than half are flood related (Douben, 2006). According to Syvitski et al. (2009), 85% of world river deltas experienced severe flooding in the past decades, with the temporary submergence of 260,000 km^2. Furthermore, flooding of urban areas is, nowadays more than ever, an issue of relevant concern. This is a consequence of the increasing world population, and of the increasing share of population residing in big cities located in flood-prone areas along major rivers or in coastal lowlands (Ceola et al., 2014; United Nations, 2015). The situation is expected to worsen in the near future owing to climate change (Dankers and Feyen, 2008; Muis et al., 2015; Whitfield, 2012).

In this view, a detailed knowledge of flooding dynamics in urban areas is important for several purposes, including urban planning, defence strategies, civil protection plans, insurance policies, etc. Numerical modelling is a key tool that has the potential to provide useful information such as water depth and flow velocity in real and hypothetical scenarios (e.g., Viero et al., 2019). Yet, modelling urban floods is a challenging task, essentially because very different spatial scales are involved in the hydrodynamic processes. Reliable analysis of flooding in large urban areas cannot disregard local effects exerted on the flow field by buildings and by a wealth of other small-scale urban features such as roads, curbs, drainage system, etc. (Meesuk et al., 2015; Mignot et al., 2013; Wang et al., 2018; Yu and Lane, 2011). Nonetheless, the excessively high precision of hyper-resolution approaches could actually mask the relatively

*Corresponding author
Email address: daniele.viero@unipd.it (Daniele P. Viero)

low accuracy owing to other uncertainty sources, for example topography errors or GIS processing, modeller choices, model parametrization, and boundary conditions (Abily et al., 2016; Cook and Merwade, 2009; Dottori et al., 2013).

A valid compromise for large-scale analyses of urban flooding is represented by the so-called porosity models. Inspired by the concept of porous medium to model urban layouts, artificial porosity is used as a statistical descriptor for the presence of buildings, which are then treated as subgrid-scale features. Preserving a reasonable accuracy even with the use of relatively coarse computational grids, such models show a great advantage in terms of computational time and resources with respect to high-resolution applications based on the classical two-dimensional Shallow Water Equations (El Kadi Abderrezzak et al., 2009; Guinot et al., 2017; Noh et al., 2018). Hence, porosity models are particularly suitable for inundation modelling in large areas, or when several runs are necessary to perform stochastic or scenario analysis, and are attracting increasing attention.

Since the first appearance of porosity models more than twenty years ago (Defina et al., 1994), different formulations have been proposed in order to capture the most salient features of the complex flow fields occurring in urban areas by using coarse grids. In the Single Porosity (SP) approach, the two-dimensional Shallow Water Equations (2D SWEs) are expressed in differential form using a single porosity field to account for buildings. SP models have been the subject of numerous works (Benkhaldoun et al., 2016; Cea and Vázquez-Cendón, 2010; Chen et al., 2012a; Defina, 2000; Ferrari et al., 2017; Finaud-Guyot et al., 2010; Guinot and Soares-Frazão, 2006; Petaccia et al., 2010; Soares-Frazao et al., 2008; Velickovic et al., 2017).

While the SP approach is isotropic in nature, urban layouts are often characterized by a marked anisotropy, with preferential flow directions owing to asymmetric building shapes and and spacing, and the alignment of buildings along streets (Sanders et al., 2008; Bruwier et al., 2018). This means that obstacles, as well as the terrain elevation at a subgrid scale, affect the direction of flow (McMillan and Brasington, 2007; Yu and Lane, 2006). In the multiple Porosity (MP) model proposed by Guinot (2012), regions characterized by different porosity, flow depth and velocity coexist within the same control volume; the scheme accounts for anisotropic effects and for head losses due to momentum exchanges. The Integral Porosity (IP) model introduced by Sanders et al. (2008) uses an integral formulation of the SWEs to properly account for discontinuities in the urban medium; a storage porosity represents the volume fraction available for mass and momentum storage, and a connectivity porosity accounts for the areal fraction of cell-sides acting on the computation of inter-cell fluxes. IP model was further improved with the introduction of a depth-dependent porosity (Özgen et al., 2015, 2016). Finally, the Dual Integral Porosity (DIP) model (Guinot et al., 2017) definitely formalizes the distinction between porosity and flux variables, with the former referring to control volumes, and the latter to boundaries; simple closure relations relate these variables to each other. In the DIP scheme, a transient momentum dissipation model is also introduced. Laboratory and numerical experiments (Kim et al., 2015) showed that the IP approach outperforms the SP one. Wave propagation properties, flux and source term models, are further improved in the DIP model (Guinot et al., 2017; Guinot, 2017b).

Unfortunately, the IP and DIP approaches are known to be markedly mesh-dependent. As already observed by Sanders et al. (2008), the IP approach is inherently mesh-dependent as the conveyance porosity is defined locally at the cell sides. While the use of suitable unstructured meshes can limit this problem (Sanders et al., 2008; Schubert and Sanders, 2012), Guinot (2017a) showed that oversensitivity to mesh design is due to a polarization of fluxes and to cell edge orientation that emerge when the flux porosity field is anisotropic. Guidelines for a proper mesh design were provided in Guinot (2017a), where it was also admitted that their fulfilment is not trivial in real-world applications.

It is interesting to observe that porosity models for urban floods have been typically implemented in the framework of Finite Volume, collocated schemes (i.e., all the conserved variables refer to the barycentre of the cell, while fluxes are evaluated at the cell sides). In the present study, a Finite Element numerical model is used (Defina, 2003; Viero et al., 2013a), in which the 2D SWEs are discretized on an unstructured staggered mesh. Water levels are defined at the grid nodes, where the continuity equation is solved, whereas triangular cells are devoted to convey fluxes according to the momentum conservation equations. Staggered mesh schemes are known to possess good conservation properties (Casulli, 2009; Perot, 2000). This Finite Element model was recently enhanced to account for anisotropic resistances using a tensor formulation to evaluate the directionally dependent bottom shear stress. It was then applied to model overland and shallow inundation flows in agricultural landscapes, where small-scale linear features (e.g., ditches) force anisotropy in the flow (Viero and Valipour, 2017). The model did not show any oversensitivity to mesh design.

The tensor formulation adopted by Viero and Valipour (2017) to account for anisotropic resistance paved the way to the development of a new, dual porosity approach for large-scale modelling of floods in urban areas. In the present subgrid model, an isotropic porosity accounts for the reduced water storage in the continuity equation, and an

anisotropic conveyance porosity is introduced in the momentum equations to compute acceleration and bottom shear stress based on the effective flow velocity. Anisotropy is accounted for as a function of the cross-sectional area actually available to conveyance in a given direction. This area, suitably normalized, closely resembles the areal conveyance porosity introduced in the IP/DIP approaches (Guinot et al., 2017; Sanders et al., 2008). However, in this case, the conveyance porosity is not defined locally at the cell interfaces, but averaged over each cell, and it is defined along principal, mutually orthogonal directions. In this way, mesh-dependency is avoided.

The numerical model is described (Section 2) and then applied to schematic and laboratory case studies (Section 3), with the aim of highlighting the strengths and the limitations of the proposed approach. These are finally discussed and summarized in Section 4.

2. The numerical model

2.1. The Finite Element numerical framework

The new dual porosity approach for urban floods is implemented in the framework of the 2DEF Finite Element hydrodynamic model (D'Alpaos and Defina, 2007; Defina, 2003; Viero et al., 2013a, 2014; Viero and Defina, 2016). The 2DEF model solves a modified version of the 2D SWEs, which is obtained through a phase averaging procedure over a Representative Elementary Area (REA) in order to deal with flooding and drying over irregular topography (Defina, 2000). Projected on the Cartesian frame (x, y), the 2D SWEs solved by the model read

$$\frac{\mathrm{D}u_x}{\mathrm{D}t} + g\frac{\partial h}{\partial x} + \frac{\tau_x}{\rho Y} - Re_x = 0 \tag{1}$$

$$\frac{\mathrm{D}u_y}{\mathrm{D}t} + g\frac{\partial h}{\partial y} + \frac{\tau_y}{\rho Y} - Re_y = 0 \tag{2}$$

$$\vartheta(h)\frac{\partial h}{\partial t} + \frac{\partial q_x}{\partial x} + \frac{\partial q_y}{\partial y} = 0 \tag{3}$$

where g is gravity, D/Dt is the material (or Lagrangian) time derivative, $\mathbf{u} = (u_x, u_y)$ is the flow velocity, h is the free-surface elevation over a datum, Y is the effective water depth defined as the volume of water per unit area (thus accounting for porosity), $\mathbf{q} = (q_x, q_y)$ is the discharge per unit width, $\boldsymbol{\tau} = (\tau_x, \tau_y)$ is the bottom shear stress, ρ is the water density. The horizontal components of Reynolds turbulent and dispersion stresses, Re, are modelled according to the Boussinesq approximation with the depth integrated model for the eddy viscosity proposed by Stansby (2003) and Uittenbogaard and van Vossen (2004):

$$\begin{aligned} Re_x &= \frac{1}{Y}\frac{\partial}{\partial x}\left(2\nu_e Y\frac{\partial u_x}{\partial x}\right) + \frac{1}{Y}\frac{\partial}{\partial y}\left[\nu_e Y\left(\frac{\partial u_x}{\partial y} + \frac{\partial u_y}{\partial x}\right)\right] \\ Re_y &= \frac{1}{Y}\frac{\partial}{\partial y}\left(2\nu_e Y\frac{\partial u_x}{\partial x}\right) + \frac{1}{Y}\frac{\partial}{\partial x}\left[\nu_e Y\left(\frac{\partial u_x}{\partial y} + \frac{\partial u_y}{\partial x}\right)\right] \\ \nu_e &= \sqrt{(2C_S^2 A_e)^2\left[2\left(\frac{\partial u_x}{\partial x}\right)^2 + \left(\frac{\partial u_y}{\partial x} + \frac{\partial u_x}{\partial y}\right)^2 + 2\left(\frac{\partial u_y}{\partial y}\right)^2\right] + (C_E u_* Y)^2} \end{aligned} \tag{4}$$

In Eq. (4), to evaluate the eddy viscosity ν_e, the Smagorinsky model is used for horizontal turbulence and the Elder model for vertical turbulence. In the last equation, A_e is the area of the computational element, u_* is the bed-shear velocity, and the two coefficients are assumed equal to $C_S = 0.2$ and $C_E = 0.07$, respectively.

The term $\vartheta(h)$ in Eq. (3) is a depth-dependent storage coefficient (Defina, 2000; Viero et al., 2014), defined as the ratio between the wet and the total area of a cell for a given water surface elevation, h.

In Eqs. (1) and (2), local and advective accelerations are lumped into the material (or Lagrangian) time derivative of the depth-averaged velocity components, taking advantage of the so-called Eulerian-Lagrangian methods in which the standard finite element procedure is combined with the method of characteristics (Defina, 2003; Giraldo, 2000; Walters and Casulli, 1998). In the model, the material time derivatives in Eqs. (1) and (2) are replaced by their finite difference formulation

$$\frac{\mathrm{D}\mathbf{u}}{\mathrm{D}t} \cong \frac{\mathbf{u} - \mathbf{u}_0}{\Delta t} \tag{5}$$

in which the subscript "$_0$" denotes a quantity evaluated at the previous time step and at the departure point, i.e., the position occupied by a fluid particle at the previous time step, located backward along the Lagrangian trajectory (Defina, 2003). With the use of Eq (5), Eqs. (1) and (2) are conveniently linearised, solved for (u_x, u_y), and substituted into the continuity equation 3, which is finally solved using an Eulerian, semi-implicit, Galerkin Finite Element scheme (Defina, 2003; Viero and Valipour, 2017).

Unlike other well-known schemes that use staggered grids (e.g., Casulli, 2009, 2015; Kramer and Stelling, 2008), in the present scheme the free surface elevation is defined at grid nodes; triangular cells link together adjacent nodes and convey fluxes as a function of quantities defined on an element-by-element basis (free-surface gradient, stress terms, etc.). The resulting staggered scheme naturally handles discontinuities in bottom elevation between adjacent elements, but is not suitable to deal with supercritical flows and shock waves, nor with rapidly varying flows (Defina et al., 2008a,b; Guinot, 2012; Viero et al., 2017).

2.2. Porosity treatment of urbanized areas

2.2.1. Isotropic storage porosity

It is worth noting that the particular form in which the model equations are expressed, naturally allows to account for storage reduction due to the presence of buildings through a proper definition of the parameter ϑ in Eq. (3).

In the context of subgrid models, it has first to be noted that the terrain elevation is assumed to vary within each computational element. To account for this variability, Defina (2000) enforced a statistically-based model for subgrid macro-roughness and expressed the wet fraction of a partially dry area analytically as

$$\eta(h) = \frac{1}{2}\left[1 + \mathrm{erf}\left(2\frac{d}{a_r}\right)\right] \tag{6}$$

where $\mathrm{erf}(\cdot)$ is the error function, $d = h - z_b$ is the mean water depth, z_b is the mean bottom elevation, and a_r is a characteristic macro-roughness height. Finally, for the h-dependent storage coefficient in Eq. (3), Defina (2000) assumed $\vartheta(h) = \eta(h)$ (Fig. 1).

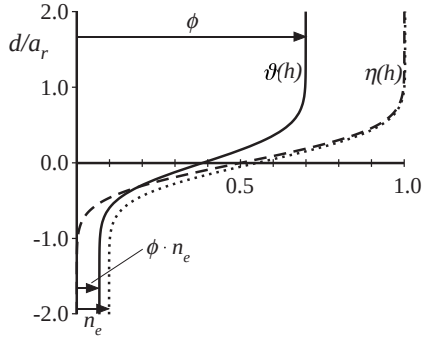

Figure 1: Dashed line denotes $\eta(h)$ (Eq. 6), dotted line represents Eq. (7), and solid line denotes $\vartheta(h)$ as a function of the non-dimensional water depth, d/a_r. In the figure, $\vartheta(h)$ is given by Eq. (8) with soil porosity $n_e = 0.1$ and storage porosity $\phi = 0.7$.

Viero et al. (2014), with the aim of modelling the hydrological response of agricultural catchments, modified the storage coefficient to account for the porosity of topsoil layer, n_e. It became

$$\vartheta(h) = n_e + (1 - n_e) \cdot \eta(h) \tag{7}$$

In the above equation, n_e acts as the lower limit for ϑ (dotted line in Fig. 1). A similar approach were used by other researchers, for example to account for the presence of "porous" obstacles in the flow field (Liang et al., 2007), to simulate the wet-dry moving boundary (Yuan et al., 2008), and for coupling surface and subsurface water flows (Kong et al., 2010).

In an urban layout, the isotropic porosity ϕ is defined as the fraction of space available to water storage (i.e., the fraction of horizontal area not occupied by buildings). Considering that buildings occupy the same area on the ground and on the topmost soil layer, the storage parameter in the continuity equation becomes

$$\vartheta(h) = \phi[n_e + (1 - n_e) \cdot \eta(h)] \tag{8}$$

where now ϕ and $\phi \cdot n_e$ are the upper and the lower limit of $\vartheta(h)$, respectively (solid line in Fig. 1).

The effects played by buildings in reducing the momentum storage are accounted for in the momentum equations (1) and (2) through the effective water depth Y, which also depends on ϑ and, in turn, on ϕ. The effective water depth Y, which is defined as (Defina, 2000)

$$Y = \int_{-\infty}^{h} \vartheta(z) dz \tag{9}$$

tends to $Y = \phi d$ when the mean water depth d is far greater than the macro-roughness height a_r (note that both the integrand and the integral in the above equation are spatially averaged quantities). By defining the discharge per unit width as $\mathbf{q} = Y\mathbf{u}$ ($\cong \phi d\mathbf{u}$), the system of equations (1)-(3), together with Eq. (8), closely resembles that of the classical single porosity (SP) model described in Guinot and Soares-Frazão (2006).

2.2.2. Anisotropic conveyance porosity

The SP model is isotropic by definition; yet, many urban layouts are characterized by markedly anisotropic patterns (Bruwier et al., 2018; Mignot et al., 2006; Sanders et al., 2008; Velickovic et al., 2017). Moreover, a fraction of the domain that is free of buildings does not contribute to transport due to the sheltering effect of buildings that results in dead zones. The SP approach can thus be enhanced with the introduction of a conveyance (or connectivity) porosity, Ψ, that scales the transport capacity (Arrault et al., 2016; Guinot et al., 2017; Sanders et al., 2008). Of course, to account for dead zones, the conveyance porosity should be taken such that $\Psi \leq \phi$, the difference ϕ - Ψ thus representing an estimate of the fraction of domain that does not contribute to transport (Sanders et al., 2008). Importantly, the conveyance porosity must account for the directional dependence that typically characterizes urban media.

The usefulness of distinguishing between storage and conveyance porosities was clearly demonstrated in many literature studies (Guinot et al., 2017; Kim et al., 2015; Sanders et al., 2008; Schubert and Sanders, 2012). However, IP and DIP schemes were implemented using collocated FV schemes, in which conserved variables (defined on an element-by-element basis) are "duplicated" at cell interfaces in order to compute fluxes; accordingly, while storage porosity used to define the conserved variables refers to control volumes (i.e., grid cells, Defina, 2000; Guinot et al., 2017), the conveyance porosity used to define fluxes only refers to cell interfaces (Guinot et al., 2017; Sanders et al., 2008). Unfortunately, the point-based assessment of the connectivity porosity makes these models suffering from oversensitivity to mesh design (Guinot, 2017a,b).

In the Finite Element staggered model used in this study, while continuity is balanced at grid nodes (storage porosity at nodes is weighted-averaged from that of surrounding elements), fluxes are defined on an element-by-element basis. Accordingly, conveyance porosity must refer to the entire cell and not to cell interfaces. This need can be seen as an opportunity to better describe the conveyance porosity field by better reflecting the connectivity properties of the urban medium within the cells and not only at the cell interfaces (Guinot, 2017a).

The estimation of an element-by-element conveyance porosity is in general not trivial for complex urban layouts, and it is beyond the scope of the present study. Here, the conveyance porosity is defined and introduced in the model under a number of simplifying hypotheses. With reference to the one-dimensional (1D) schematic case depicted in Fig. 2a, Q denotes the total discharge and $q = Q/W$ is the discharge per unit width, phase-averaged over the entire area of the cell (Defina, 2000). The presence of buildings (shaded areas in Fig. 2a) results in a channel contraction, where the actual flow velocity is

$$u_c = \frac{Q}{d\,w} = \underbrace{\frac{Q}{W}}_{=q} \cdot \underbrace{\frac{W}{w}}_{=1/\Psi} \cdot \underbrace{\frac{1}{d\,\phi}}_{=1/Y} \cdot \phi = \frac{\phi}{\Psi}\frac{q}{Y} \tag{10}$$

In Eq. (10), $\Psi = w/W$ is the conveyance porosity, which is assumed equal to the width ratio of the channel contraction (Defina and Viero, 2010).

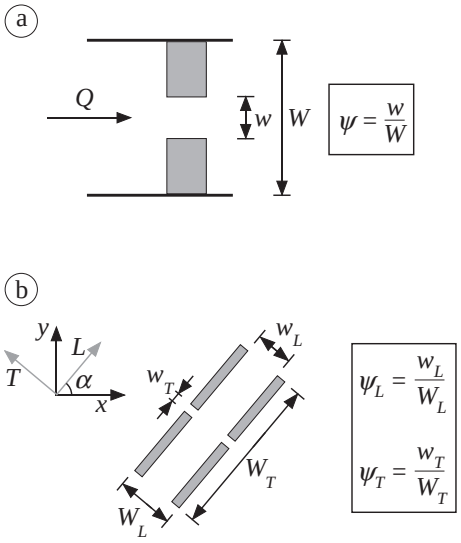

Figure 2: Schematic definition of the conveyance porosity, Ψ, for a one-dimensional case (panel a) and for a two-dimensional case (panel b). Shaded areas denote buildings.

Similarly to the previous 1D case, in the 2D schematic case of Fig. 2b the conveyance porosity can be estimated along two principal, mutually orthogonal directions (say $L - T$), for which the conveyance porosity is respectively maximum (Ψ_L) and minimum (Ψ_T). Along each principal direction, conveyance porosities are evaluated with reference to the narrowest cross-section (Fig. 2b); this allows to write the components of the effective flow velocity as

$$u_{c_L} = \frac{\phi}{\Psi_L}\frac{q_L}{Y}; \qquad u_{c_T} = \frac{\phi}{\Psi_T}\frac{q_T}{Y} \tag{11}$$

2.2.3. Momentum equations in terms of effective velocity

In the dual porosity subgrid model, the momentum equations (1) and (2) are expressed in terms of effective velocity $\mathbf{u_c}$, with significant consequences for the evaluation of temporal and spatial accelerations (lumped in the first terms of Eqs. (1) and (2)) and of energy dissipation due to bottom shear stress (the third terms of Eqs. (1) and (2)).

The use of the velocity at the contraction, $\mathbf{u_c}$, in the momentum equations is equivalent to assume that water flows within the narrowest cross-section for the length of the entire computational cell. This is a simplifying hypothesis already assumed in other studies (Bruwier et al., 2017; Chen et al., 2012a; Dottori and Todini, 2013; Ferrari et al., 2018), and justified by the fact that energy dissipation varies quadratically with the velocity and linearly with the length of the path; most of the dissipation occurs where velocity is greater, and the jet developing downstream of the contraction causes the velocity to decrease slowly along the flow direction (i.e., the effective length of the narrowest section is longest than its purely geometrical length).

As the conveyance porosity is directionally dependent, it is convenient to resort to tensor notation, so as to express the effective velocity as

$$\mathbf{u_c} = \mathbf{A}\mathbf{q} \tag{12}$$

with $\mathbf{u_c} = (u_{cx}, u_{cy})$, $\mathbf{q} = (q_x, q_y)$, and $\mathbf{A}$ a second-order tensor whose principal components are

$$A_L = \frac{\phi}{\Psi_L Y} \qquad \text{and} \qquad A_T = \frac{\phi}{\Psi_T Y} \tag{13}$$

If the principal directions are rotated by some angle α relative to the model frame (Fig. 2b), the components of $\mathbf{A}$ descend from the transformation law of a second-order tensor (Graebel, 2007)

$$\mathbf{A} = \begin{bmatrix} A_{xx} & A_{xy} \\ A_{xy} & A_{yy} \end{bmatrix} = \begin{bmatrix} A_L \cos^2\alpha + A_T \sin^2\alpha & (A_L - A_T)\cos\alpha \sin\alpha \\ (A_L - A_T)\cos\alpha \sin\alpha & A_L \sin^2\alpha + A_T \cos^2\alpha \end{bmatrix} \tag{14}$$

To properly account for the actual connectivity of the urban medium, the flow accelerations are expressed in terms of effective velocity. Practically, the material derivative of the depth-averaged flow velocity (see Eq. 5) becomes

$$\frac{\mathrm{D}\mathbf{u_c}}{\mathrm{D}t} \cong \frac{\mathbf{u_c} - \mathbf{u}_{c0}}{\Delta t} = \frac{\mathbf{Aq} - \mathbf{Aq}_0}{\Delta t} \tag{15}$$

Similarly, the resistance terms $\boldsymbol{\tau} = (\tau_x, \tau_y)$ are introduced in the model in tensor form (Viero and Valipour, 2017)

$$\frac{\boldsymbol{\tau}}{\rho g Y} = \mathbf{Rq} \tag{16}$$

with $\mathbf{R}$ a second-order tensor. By denoting with n_L and n_T the Manning roughness coefficients along, respectively, the L and T directions, the principal components of the tensor $\mathbf{R}$ are

$$R_L = \frac{\tau_L}{\rho g Y} = \frac{n_L^2 q}{\Psi_L^2 H^{10/3}} \qquad \text{and} \qquad R_T = \frac{\tau_T}{\rho g Y} = \frac{n_T^2 q}{\Psi_T^2 H^{10/3}} \tag{17}$$

where q is the modulus of the phase-averaged discharge per unit width. H is a parameter derived from (Y/ϕ) according to Appendix A in Defina (2000) and used to account for the effect of sub-grid scale macro-roughness on bottom shear stress.

Again, if the principal directions are rotated by some angle α relative to the model frame (Fig. 2b), the components of $\mathbf{R}$ become

$$\mathbf{R} = \begin{bmatrix} R_{xx} & R_{xy} \\ R_{xy} & R_{yy} \end{bmatrix} = \begin{bmatrix} R_L \cos^2\alpha + R_T \sin^2\alpha & (R_L - R_T)\cos\alpha \sin\alpha \\ (R_L - R_T)\cos\alpha \sin\alpha & R_L \sin^2\alpha + R_T \cos^2\alpha \end{bmatrix} \tag{18}$$

From here on, the model implementation closely resembles that presented in Viero and Valipour (2017) and is detailed in Appendix A.

2.3. Additional remarks on the dual porosity subgrid model

Some aspects of the dual porosity subgrid model presented above need to be further discussed.

The model does not account for building drag, which could be included using a formulation of those presented and discussed in other studies (Guinot et al., 2017; Guinot, 2017b; Velickovic et al., 2017). However, since the estimation of drag coefficients mostly relies on calibration (Guinot et al., 2017; Velickovic et al., 2017), they are not considered in this study, whose main aim is to check the ability of the subgrid dual porosity model in reproducing reference results when porosities parameters are derived from geometrical information only.

The model does not account for transient momentum dissipation due to shock wave reflections that occur when obstacles force a supercritical flow to change its direction (Guinot, 2012, 2017b; Guinot et al., 2017, 2018; Viero et al., 2013b). This is consistent with the fact that the Finite Element model is not intended to deal with supercritical flows nor with shock waves. It is well known, in fact, that shock-capturing schemes are needed to produce reliable results at the local scale when the Froude number exceeds one, or when analysing markedly unsteady flows such as dam-break flood waves (Teng et al., 2017). Nonetheless, in terms of broader results, models that are unable to deal with supercritical flows (for instance, Finite Element, diffusive-wave, or raster-cell models) were shown to give similarly good results (Dottori and Todini, 2013; Hunter et al., 2008; Neal et al., 2009; Neelz and Pender, 2007).

More importantly, the effectiveness of the tensor formulation for the conveyance porosity, the existence of (and the possibility of detecting) two principal directions of maximum and minimum conveyance, and the computation of hydraulically significant conveyance porosities in real urban layouts, are questionable and challenging tasks that undoubtedly deserve further investigation. As a side note, the assumption of mutually orthogonal principal directions in the definition of conveyance porosity can be removed by considering a different angle for each principal axis (Guinot et al., 2017).

Finally, the present model can be seen as an improvement of the multi-layered model proposed by Chen et al. (2012b), in that the present model solves the full 2D SWEs and allows modelling blocking features not aligned with the

main axes of the model. The detection of blocking feature from high-resolution LiDAR surveys can be done following the procedures proposed by Hodges (2015).

3. Model results

The dual porosity model presented in Sect. 2 is tested considering three different schematic applications (Tests 1, 2, and 3), in which the results from the dual porosity model are compared with those of a "reference simulation", i.e., a refined solution in which the buildings are explicitly resolved using the "building hole" technique (Schubert and Sanders, 2012). In "Test 4", the benchmark consists in reproducing a laboratory experiment reported in Velickovic et al. (2017).

It has to be stressed that, in all the numerical applications showed thereafter, the additional parameters needed by the dual porosity model (i.e., the storage porosity ϕ, the conveyance porosities Ψ_L and Ψ_T, and the rotation angle α) have been derived geometrically, and not by calibration.

3.1. Steady flow through a schematic urban layout

In the first application (Test 1), an array of 2×3 aligned buildings (Fig. 3) is placed at the centre of a tilted plane (bottom slope of 0.065% southward, Manning roughness coefficients $n_L = n_T = 0.0286$ m$^{-1/3}$s, macro-roughness height $a_r = 0.1$ m). The storage and conveyance porosities are assumed constant within the area occupied by the building array, and are estimated geometrically. Within the exact limits of the urban layout, the urban porous medium is characterized by a storage porosity $\phi = 0.3$ and, following Fig. 2b, by conveyance porosities $\Psi_L = 0.25$ and $\Psi_T = 0.067$, with $\alpha = 50°$. A constant inflow discharge of 50 m^3/s is prescribed at the centre of the northern boundary, and a suitable rating curve is imposed at the southern boundary. Simulations are protracted until steady state conditions are attained.

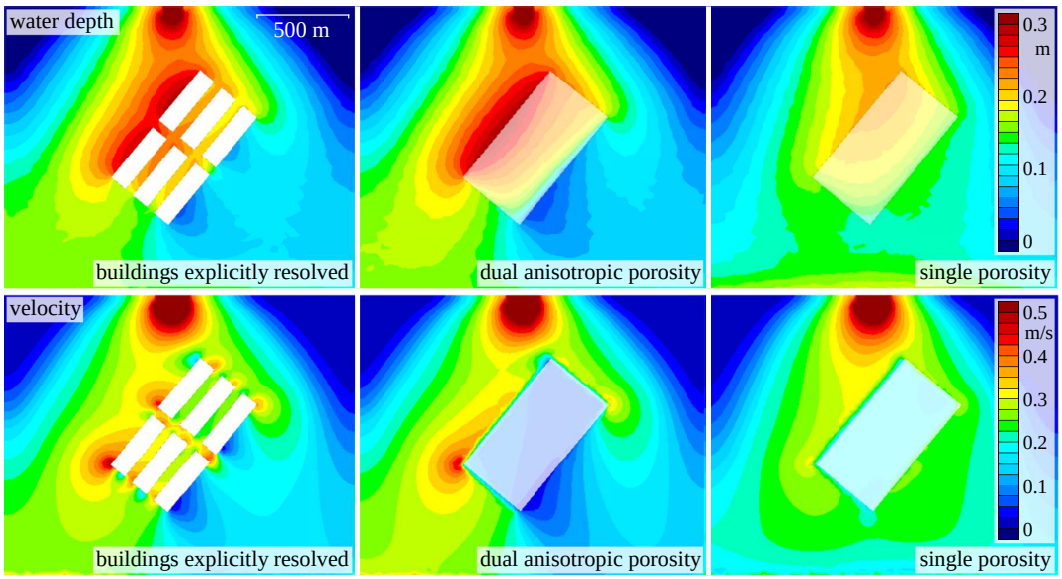

Figure 3: Test 1: steady flow through a schematic urban layout simulated using a "building hole" high resolution grid (left), the dual porosity model (centre) and the single porosity model (right). The results are reported in terms of flow depth (upper panels) and velocity (lower panels).

In this test, a comparison is drawn between the dual porosity subgrid model, the reference simulation, and also with the results from the single porosity (SP) version of the the model, which is obtained by simply assuming $\Psi_L = \Psi_T = \phi$. The reference solution is obtained using a suitably refined mesh, characterized by cell-sides about 5 m long. Based on a set of preliminary simulations, no significant improvements in the numerical solution are expected from a further refinement of the mesh. The dual and single porosity models are run over a much coarser mesh, with cell-sides about 20 m long within the patch of urbanized area. Note that each building in the urban layout has dimensions 100×350 m.

The model results are shown in Fig. 3. The results from the refined solution (left panels) show that the flow is mainly driven westward by the presence of buildings, and that the local maximum of flow velocity occurs downstream of the urban layout at the western corner. From a macroscopic point of view, the solution from the dual porosity model (central panels) closely resembles that of the reference simulation (left panels). On the contrary, the SP approach (right panels) is unable to correctly characterize the markedly anisotropic flow field that is generated by the array of aligned buildings.

3.2. Unsteady flow through a street grid

In the second application (Test 2), a hypothetical flood wave (Fig. 4) is routed over an initially dry, tilted plane. The street grid extracted from a real urban layout is placed at the centre of the plane (Fig. 5, bottom slope of 0.065% southward, Manning roughness coefficients $n_L = n_T = 0.0154$ m$^{-1/3}$s along the streets and $n_L = n_T = 0.0286$ m$^{-1/3}$s elsewhere, macro-roughness height $a_r = 0.1$ m). Flooding simulation in relatively dense urban layouts has been successfully performed considering only the street grid by, e.g., Mignot et al. (2006).

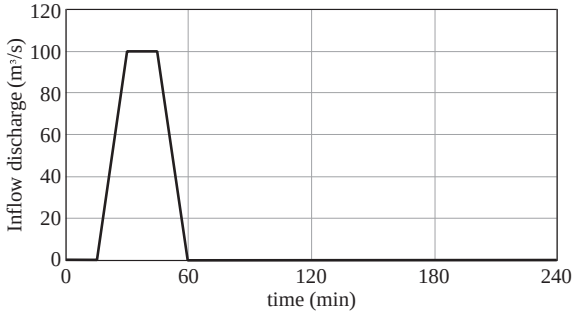

Figure 4: Test 2: discharge hydrograph prescribed as inflow boundary condition.

As in Test 1, the storage and conveyance porosities are assumed constant within the patch of urban area, and are estimated geometrically. Specifically, the storage porosity is computed as the fraction of street area to the total urbanized area, which gives $\phi = 0.22$; the conveyance porosities are computed in agreement with the definitions sketched in Fig. 2b. The values obtained as the ratio between the width of the crossed streets to the total width, at the narrowest cross-sections, are $\Psi_L = 0.10$ and $\Psi_T = 0.08$; principal axes are oriented at $\alpha = 65°$ to the model frame. The discharge hydrograph (Fig. 4) is prescribed at the centre of the northern boundary, and a suitable rating curve is imposed at the southern boundary.

The reference solution is obtained using a suitably refined mesh, characterized by cell-sides about 3 m long. A set of preliminary simulations suggested that no significant improvements in the numerical solution are expected from a further refinement of the mesh. The single and the dual porosity models are run over a mesh with cell-sides about 15 m long within the patch of urbanized area, i.e., much coarser than that used in the reference simulation.

The results from both the porosity models (middle and lower panels in Fig. 5) compare well with those obtained by solving the classical 2D SWEs over a high-resolution grid (upper panels in Fig. 5), both in terms of water depth and of the timing of flooding. The performance of the two subgrid models are similar because the street grid is characterized by a slight anisotropy (Ψ_L and Ψ_T are close to each other). The main difference between the single and dual porosity models is that the dual porosity approach slightly underestimates the propagation speed of the wetting front within the urban layout, whereas the single porosity approach slightly underestimates the flow resistance.

3.3. Unsteady flow in urban areas with different storage and conveyance porosities

In this third application (Test 3), the same flood wave used in Test 2 (Fig. 4) is routed over a patch of urban area in which storage and conveyance porosities are significantly different from each other. This may occur for example in middle-density urban areas where houses and buildings are placed within relatively ample walled gardens. While water is temporarily stored in gardens and courtyards in the course of a flooding event, only the streets actively contribute to conveyance.

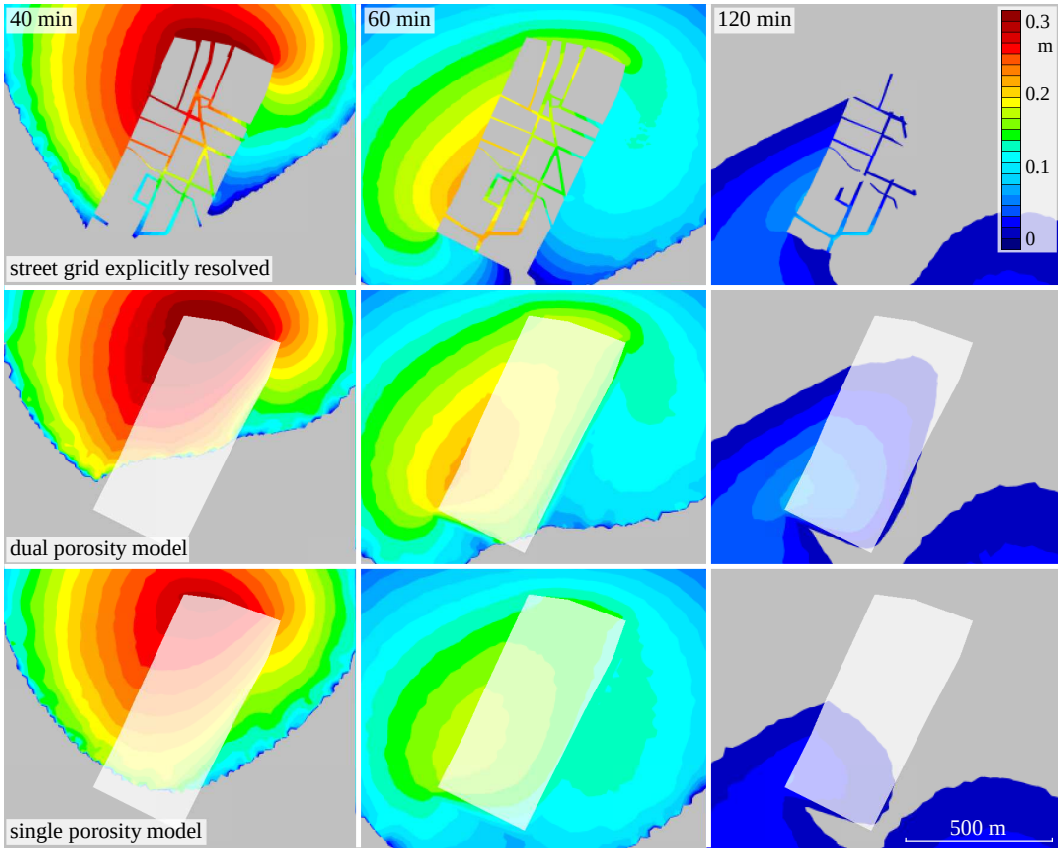

Figure 5: Test 2: unsteady flow through the street grid of a real urban layout simulated using a high resolution grid (upper panels), the dual porosity model (middle panels), and the single porosity model (lower panels). The results are reported in terms of flow depth at different time instants.

To test the ability of the subgrid dual porosity approach in such a context, gardens and courtyards are added to the patch of urban area previously analysed in Test 2 (Fig. 6). In the reference simulation, buildings and garden walls are treated according to the "building hole" technique (Schubert and Sanders, 2012). Again, porosities are assumed constant within the patch of urban area, and are estimated geometrically. In this Test 3, the storage porosity accounts for the area occupied by both the streets and the garden yards, resulting equal to $\phi = 0.78$ (a far greater value than in Test 2, in which $\phi = 0.22$); as only the streets are deputed to net conveyance, conveyance porosities are the same as in the previous Test 2, i.e., $\Psi_L = 0.10$ and $\Psi_T = 0.08$, with $\alpha = 65°$. As in Test 2, the bottom slope is 0.065% southward, the Manning roughness coefficients are $n_L = n_T = 0.0154$ m$^{-1/3}$s along the streets and $n_L = n_T = 0.0286$ m$^{-1/3}$s elsewhere, and the macro-roughness height is $a_r = 0.1$ m.

Figure 6: Test 3: patch of urban area characterized by the presence of houses (grey areas) and garden yards surrounded by walls (black lines).

The model results are plotted in Fig. 7 at three different times (40, 60, and 120 minutes). The upper panels show the water depth obtained in the reference solution, in which the classical SWEs are solved over a mesh of about 63,000 triangular elements (cell-sides about 3 m long within the urban area). It can be seen that the urban patch produces significant resistances, which retard the flood wave propagation and cause a larger water depth in the upstream part of the domain. The middle panels show the results from the dual porosity model proposed in this study, which is run over a coarse mesh of about 9,000 triangular elements (cell-sides about 15 m long within the urban area). The subgrid, dual porosity model well reproduces the macroscopic effects exerted by the urban layout on the flood wave, and successfully captures the most salient features of the flow field in the different phases of the flooding event. The lower panels of Fig. 7 show the model results obtained on the same coarse mesh using a single porosity (SP) approach, i.e., by assuming $\Psi_L = \Psi_T = \phi = 0.78$. In this case, resistances are significantly underestimated by the model, which provides unreliable results compared to both the reference simulation and the dual porosity model.

In Fig. 8, the results from the different approaches are compared in terms of water discharge flowing through three cross-sections located along the urban area (cross-sections are indicated as S1, S2, and S3 in the central panel of Fig. 7). With respect to the reference simulation (thick solid lines in Fig. 8), the SP approach (dotted lines in Fig. 8) overestimates the discharge hydrographs at all the three cross-sections (flow rates are up to three times greater than in the reference simulation). Resistances are underestimated in the SP approach; in fact, while the single porosity is set to correctly reproduce the storage capacity of the urban medium, it does not allow accounting for the reduced

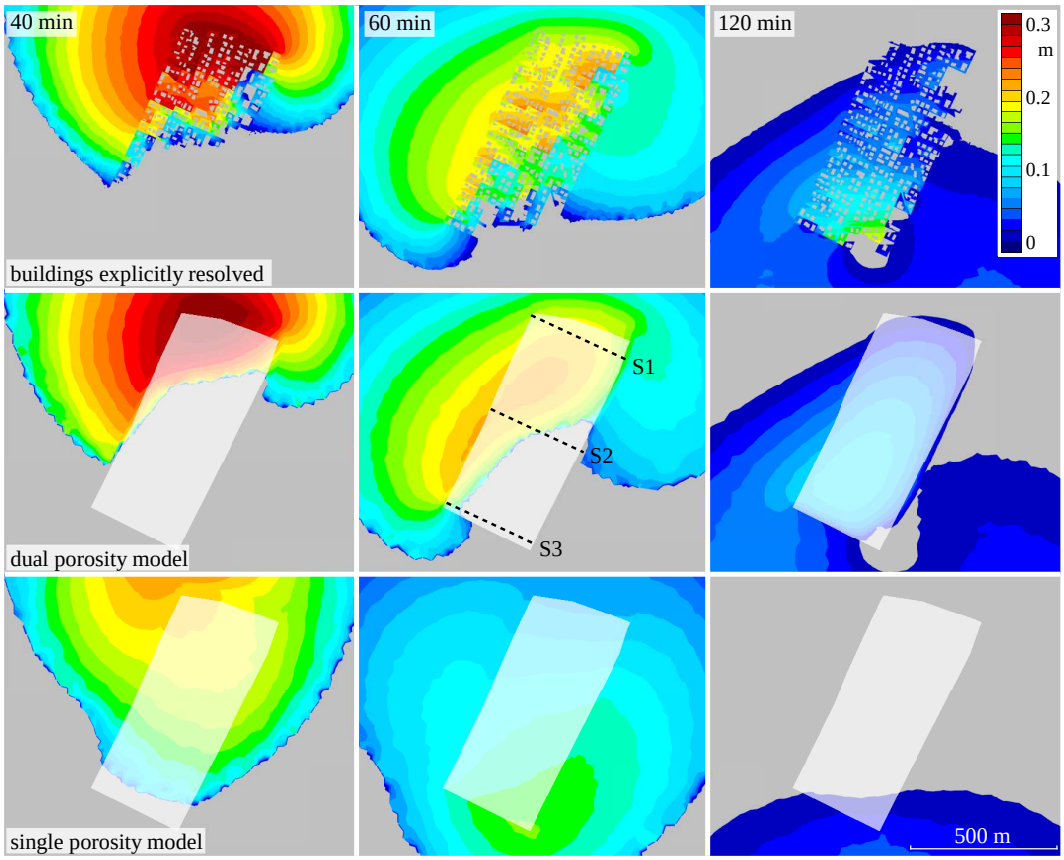

Figure 7: Test 3: unsteady flow through an urban layout with buildings and garden yards surrounded by walls, simulated using a high resolution grid (upper panels), the dual porosity model (middle panels), and the single porosity approach (lower panels). The results are reported in terms of flow depth at different time instants.

connectivity owing to the garden walls. The dual porosity approach (dashed lines in Fig. 8) well reproduces the overall trend of discharges at the three cross-sections. The discrepancies between the results from the dual porosity approach and the reference simulation can be explained considering that the sub-grid approach disregards important processes that affect the flow dynamics at the local scale, for example the time actually needed by water to fill garden-yards characterized by relatively small openings.

Finally, to test the mesh-independence of the proposed approach, two additional simulations are run with the dual porosity model using different meshes with approximately the same resolution (Fig. 9). The propagation speed of the wetting front and the flow field features are preserved notwithstanding the kind of mesh actually used. The mesh independence is confirmed also by some additional simulations (not shown in the paper) in which the dimensions of the structured computational elements within the urban layout are doubled in the L direction, and the diagonals are swapped.

3.4. Comparison with laboratory experiment under steady flow conditions

As a final test, the performance of the dual porosity model is evaluated with respect to one of the laboratory experiments described in Velickovic et al. (2017). It has to be said that the flow conditions in this "Test 4" are partly beyond the scope of the Finite Element model used in the present study. In fact, the idealized urban layout here considered forces subcritical to supercritical transitions in the flow (Froude number, $\mathsf{F} = |\mathbf{u}| \,/\, \sqrt{gd}$, up to about 2.0 is found in the simulated flow field), which entails the occurrence of hydraulic jumps and oblique shock waves. Such an application can be viewed as an opportunity to shed light on both the strengths and the limitations of the present model.

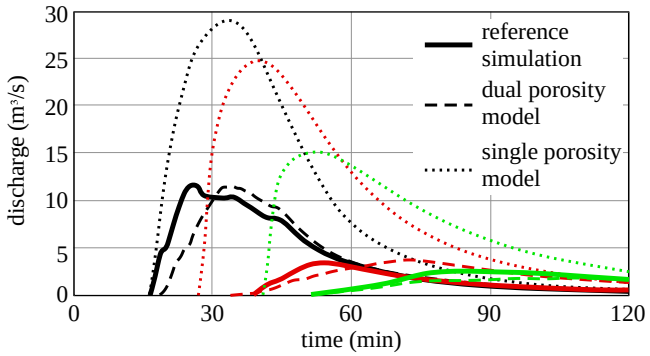

Figure 8: Test 3: water discharge computed in the reference simulation (solid lines), with the dual porosity subgrid model (dashed lines) and with the single porosity approach (dotted lines) at the three cross-sections located in the central panel of Fig. 7 (S1 in black, S2 in red, S3 in green).

Among the many urban layouts tested by Velickovic et al. (2017), the "layout B wide rotated" (Fig. 10) is here chosen. In the experimental set-up, Velickovic et al. (2017) placed an array of 5×5 square wooden blocks at the centre of a 3.6 m wide flume, in order to represent buildings (Fig. 10a). The blocks formed a network of perpendicular streets with different widths along, respectively, the L and the T principal directions (Fig. 10b). The selected experiment is particularly suitable to test the present model for a twofold reason, i) the pattern of idealized buildings is characterized by anisotropy (Fig. 10b) and, ii) the mutually orthogonal principal directions ($L-T$), as determined by the orientation of the streets, are rotated clockwise by 22.5 degrees with respect to the direction of the main channel (i.e., the x axis of the model frame).

As in the numerical experiments described above, and similarly to Velickovic et al. (2017), the parameters of the dual porosity approach are assumed constant within the patch of urban area, and are estimated geometrically. According to the dimensions reported in Fig. 10b, the storage porosity is $\phi = 0.4375$ (actually, this parameter does not play any significant role in this test as the comparison with experimental data is drawn under steady state conditions). According to the definitions sketched in Fig. 2b, the conveyance porosities are computed as the ratio between the width of the streets to the total width of the urban layout along the L and T directions, to give $\Psi_L = 0.2647$ and $\Psi_T = 0.1525$; principal axes are oriented at $\alpha = -22.5°$ to the model frame.

Considering that the flume is characterized by smooth walls, Manning roughness coefficients are assumed equal to $n_L = n_T = 0.01$ m$^{-1/3}$s as in Velickovic et al. (2017). The macro-roughness height is $a_r = 0.001$ m; in this way, the subgrid model for irregular topography plays a negligible role on the computations.

In Velickovic et al. (2017), the "layout B wide rotated" is tested with two different flow discharges, respectively Q=75 and Q=100 l/s; here, only Q=75 l/s is considered, as for Q=100 l/s the maximum Froude numbers are significantly larger, and the overall flow conditions become prohibitive for the Finite Element model.

The numerical simulations, starting with water at rest, are protracted in time until steady state conditions are attained. First, the classical SWEs are solved over a refined computational mesh with cell-sides about 0.02 m long within the patch of urban area. The computed water surface profiles are shown in Fig. 11 (blue lines), where they are compared with experimental data from Velickovic et al. (2017) (black lines). Both the modelled and the measured profiles are extracted along Profile 1 (panel a) and Profile 4 (panel b); the location of these profiles are shown in the plan view of Fig. 10. The model results are in fair agreement with experimental data, yet the water depth upstream of the urban layout is underestimated.

As a first remark, the mesh used in the present study is by far coarser than that used by Velickovic et al. (2017) to simulate the experimental data successfully. Indeed, it has to be recalled that the Finite Element numerical scheme is not intended for high-resolution computation of rapidly varying (in space as in time) flows. A further increase in the mesh resolution can only be seen as a theoretical exercise, which is meaningless in terms of practical applications of the present Finite Element model. Moreover, the numerical scheme here used is not expected to deal with supercritical flows effectively.

The dual porosity approach presented in Sect. 2.2 is then applied using a coarser mesh with cell-sides about 0.1 m long within the patch of urban area. Compared with experimental data, the results from the dual porosity approach (red

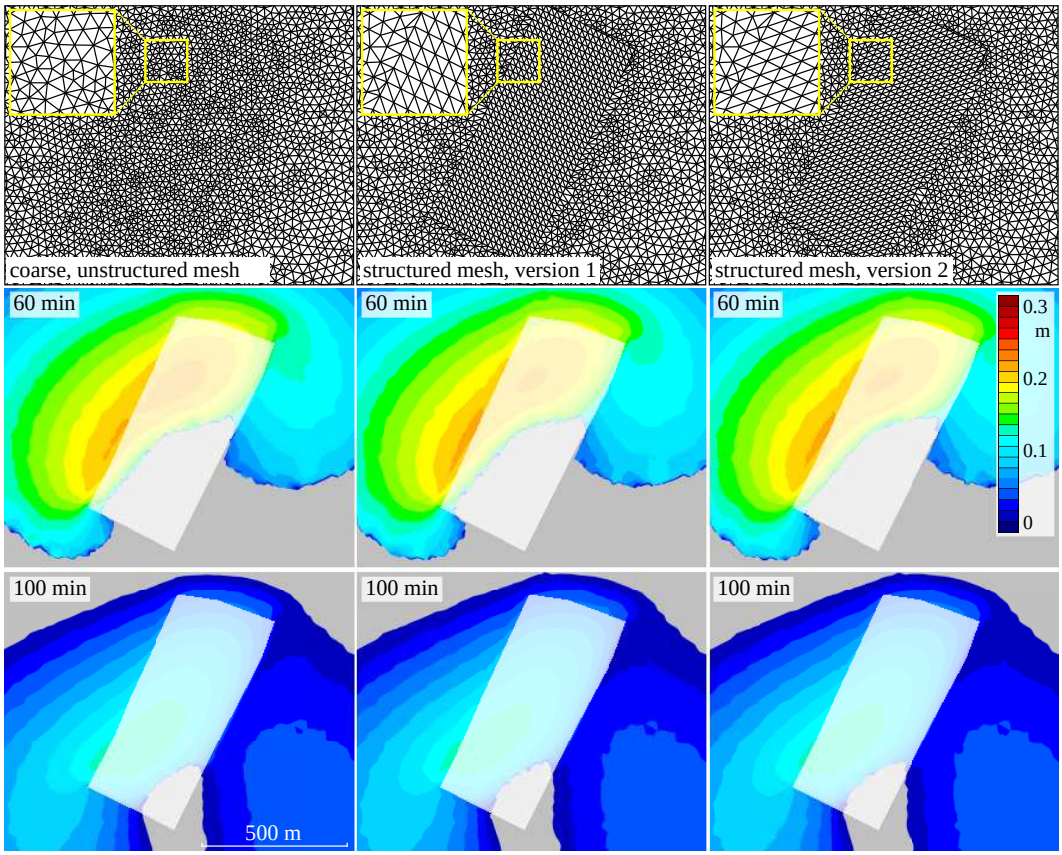

Figure 9: Test 3: unsteady flow through an urban layout with buildings and garden yards surrounded by walls, simulated using the dual porosity model on different meshes with the same resolution (upper panels). The results are reported in terms of flow depth at 60 min (middle panels) and at 100 min (lower panels).

lines in Fig. 11) are significantly poorer than those obtained by solving the classical SWEs over the finer mesh. This is in line with Velickovic et al. (2017), who also obtained considerably poorer results using their subgrid model based on directional dependent drag coefficients that were calibrated using data from different experimental conditions (see Fig. 20a,b in Velickovic et al., 2017). The reason why the results from the dual porosity model are so unsatisfactory is investigated in the following.

It has to be noted that the two additional blocks placed beside the idealized urban layout to prevent the flow from by-passing it (black areas in Fig. 10a) significantly affect the flow field. Practically, water surface elevation is much higher upstream of these blocks than just downstream of them. A significant fraction of water is expected to flow through the shorter paths linking the upstream to the downstream part of the flume (red solid lines in Fig.12); along these lines, the mean free-surface gradient is in fact the largest. However, both these paths are characterized by narrow branches (those aligned with the T direction) and by 90° bends, which are known to cause significant head losses (Arrault et al., 2016; El Kadi Abderrezzak et al., 2011; Luo et al., 2018; Mignot et al., 2008; Rivière et al., 2011, 2014; Weber et al., 2001). Hence, most of the water flows along the wider streets, i.e., along the L principal direction (Fig. 10).

The above consideration holds for the experimental setup and also for the numerical results obtained by solving the classical SWEs over the refined mesh. The picture is dramatically different when using subgrid porosity models. As porosity parameters are kept constant within the entire patch of urban area, water can flow through the area occupied by the two green blocks in Fig. 12 experiencing the same resistance it experiences elsewhere in the urban area, i.e., water can flow through significantly shorter and straight paths than in the real case. This entails a significant reduction of the overall resistance, and thus a lower water surface elevation upstream of the urban layout.

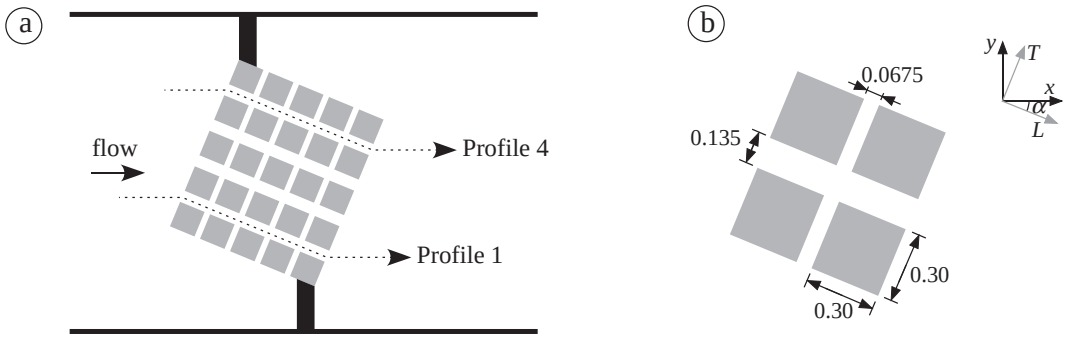

Figure 10: Test 4: plane view of the "layout B wide rotated" as described in Velickovic et al. (2017). a) The urban layout located at the center of the flume, with gray areas denoting buildings and black areas denoting two additional blocks placed beside the idealized urban layout to prevent the flow from by-passing it. b) Street width and dimensions of the squared blocks used to simulate buildings (in meters).

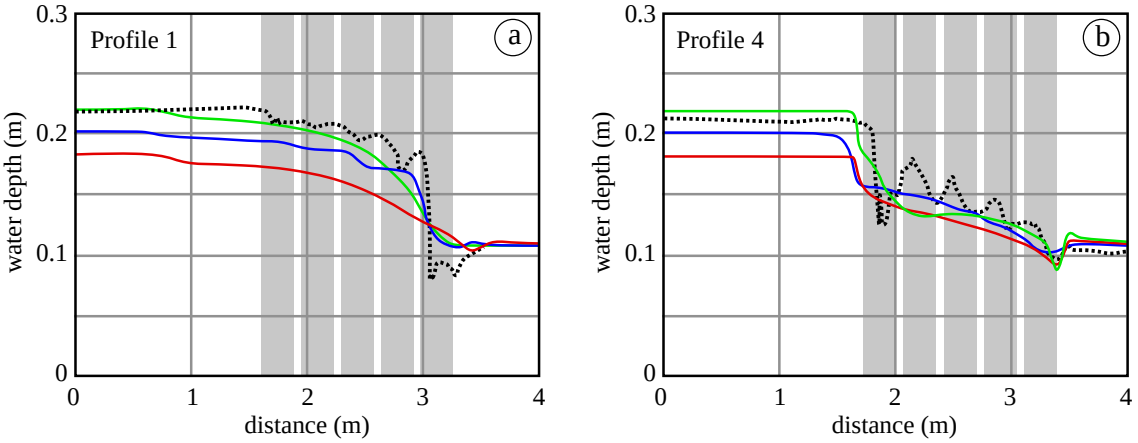

Figure 11: Test 4: water depth profiles along profile 1 and 4 (panel a and b, respectively) for the "layout B wide rotated" laboratory experiment described in Velickovic et al. (2017). The black lines denote measured experimental data. Model results refer to classical SWEs solved using a high resolution grid (blue lines) and to the dual porosity model (red lines); green lines are obtained by excluding from the computational mesh the two buildings (green squares in Fig. 12) adjacent to the additional blocks.

To prove this fact, an additional simulation is run by excluding from the mesh the computational elements covering the two green blocks in Fig. 12. In this way, the shortest paths from the upstream to the downstream part of the flume are similar in the simulation relying on the subgrid models as in the experiments. The model results, shown as green solid lines in Fig. 11, well reproduce the measured water surface profiles from a macroscopic point of view.

The need of modifying the computational mesh to obtain reliable results highlights a crucial aspect in the use of subgrid models for urban areas. Specifically, the flow field cannot be well reproduced using a subgrid approach (which in fact provide only a macroscopic description of the flow field) when the flow field is crucially affected by hydrodynamic effects acting locally at the building spatial scale.

4. Discussion and conclusions

In the present study, a dual porosity model for urban floods was developed and implemented within the framework of a Finite Element numerical scheme that solves the Shallow Water Equations on unstructured, staggered meshes. It was then validated by comparing the model results with numerical reference solutions and with data from a laboratory experiment.

Undoubtedly, the model presented in this study has a number of limitations, owing partly to the numerical framework in which the subgrid porosity model has been implemented, and partly to the subgrid dual porosity model

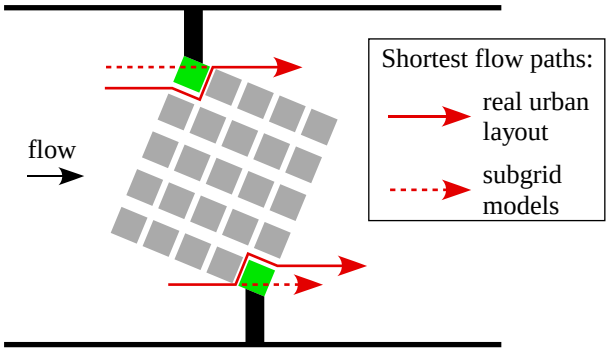

Figure 12: Test 4: shortest flow paths linking the upstream with the downstream part of the flume in the "layout B wide rotated" (red solid lines) and in the subgrid model representation when using constant porosity coefficients within the urban area (red dashed lines). The two buildings coloured in green are then excluded from the computational mesh in order to highlight the role played by the change in shorter paths when passing from the explicit simulation of buildings to the use of the subgrid model.

itself. Concerning the first point, the Finite Element numerical scheme used in this study is neither suitable to deal with shock waves, nor with rapidly varying flows. It is in fact well-known that, in the case of supercritical flows, shock capturing models solving the full SWEs must be used to account for depth and velocity variations at the building scale (Costabile et al., 2017; Sanders et al., 2008). As for the second point, the porosity treatment of the urban medium is likely too simplistic to capture the complexity of real urban settlements under general conditions. The use of two principal directions to model conveyance porosity may reveal as a poor framework to characterize the actual directional dependence of resistance due to buildings and obstacles. For example, in urban layouts with aligned buildings, resistances are greater when the flow direction is not aligned with any of the principal directions (i.e., the street directions); this is due to building drag, head losses in crossways and, on average, longer pathways. Suitable amplification coefficients could be introduced that depend on the flow direction, similar to that proposed by Velickovic et al. (2017) and discussed by Guinot (2017b).

Moreover, for real urban layouts, the evaluation of effective values of conveyance porosity is undoubtedly a hard task from both the geometric and hydraulic points of view. In the present study, porosity values and principal directions were determined at a district level. This choice was justified by the fact that the considered urban layouts were relatively small and their properties quite homogeneous. In principle, porosities and principal directions could be evaluated from the underlying geometry at a cell level, i.e., on an element-by-element basis. Further research is needed.

Notwithstanding these limitations, the results provided by the dual porosity model are promising. The comparison with numerical reference simulations obtained by solving the classical 2D SWEs on high-resolution grids showed that the dual porosity model accounts for the effects exerted by urban layouts on the flow field properly, and without the need of calibration. The use of computational meshes with different resolutions confirmed that the dual porosity subgrid model is not oversensitive to mesh design, also in presence of anisotropic porosity fields. The comparison with laboratory experiments confirmed the effectiveness of the proposed model, even if the simulated conditions were partly beyond the scope of the Finite Element model owing to the presence of patches of supercritical flows.

Acknowledgements. Francesco Ballarin is gratefully acknowledged for carrying out preliminary simulations and model testing.

Appendix A. Numerical model implementation.

Following Defina (2003) and Viero and Valipour (2017), convection is treated using a semi-implicit mixed Eulerian-Lagrangian approach. In Eqs. (1) and (2), the material derivatives are replaced by their finite difference formulation according to Eq. (15), and the energy dissipation due to bottom shear stress is expressed as in Eq. (16). Suitably rearranged, Eqs. (1) and (2) become

$$
\begin{aligned}
C_1 q_x + C_2 q_y &= -\frac{\partial h}{\partial x} + F_x \\
C_2 q_x + C_3 q_y &= -\frac{\partial h}{\partial y} + F_y
\end{aligned}
\tag{A.1}
$$

where

$$
\begin{aligned}
C_1 &= \frac{A_{xx}}{g\Delta t} + R_{xx} \\
C_2 &= \frac{A_{xy}}{g\Delta t} + R_{xy} \\
C_3 &= \frac{A_{yy}}{g\Delta t} + R_{yy} \\
F_x &= \frac{u_{cx0}}{g\Delta t} + \frac{1}{gY}\left(Re_{xx} + Re_{xy}\right) \\
F_y &= \frac{u_{cy0}}{g\Delta t} + \frac{1}{gY}\left(Re_{xy} + Re_{yy}\right)
\end{aligned}
\tag{A.2}
$$

In the above equations, the effective velocity at the departure point along the Lagrangian trajectory, $\mathbf{u}_{c0} = (u_{cx0}, u_{cy0})$ (see Sect. 2.1 and Defina, 2003), can be evaluated as $\mathbf{u}_0 = \mathbf{A}\mathbf{q}_0$, where the flow rate per unit width $\mathbf{q}_0$ again refers to the departure point at the previous time step.

The flow rates per unit width q_x and q_y can be isolated from Eqs. (A.1), to yield

$$
\begin{aligned}
q_x &= \Psi_{xx}\frac{\partial h}{\partial x} + \Psi_{xy}\frac{\partial h}{\partial y} + \Phi_x \\
q_y &= \Psi_{yx}\frac{\partial h}{\partial x} + \Psi_{yy}\frac{\partial h}{\partial y} + \Phi_y
\end{aligned}
\tag{A.3}
$$

where

$$
\begin{aligned}
\Psi_{xx} &= \frac{-C_3}{C_1 C_3 - C_2^2} \\
\Psi_{xy} &= \frac{C_2}{C_1 C_3 - C_2^2} = \Psi_{yx} \\
\Psi_{yy} &= \frac{-C_1}{C_1 C_3 - C_2^2} \\
\Phi_x &= -\Psi_{xx} F_x - \Psi_{xy} F_y \\
\Phi_y &= -\Psi_{xy} F_x - \Psi_{yy} F_y
\end{aligned}
\tag{A.4}
$$

Under the assumption of slow varying flow, the momentum equations along the $x-$ and $y-$axes are easily linearised by estimating the above coefficients Ψ and Φ at the previous time step. Alternatively, a mildly non-linear system can be efficiently solved following Casulli and Zanolli (2012).

The flow rates q_x and q_y, as they appear in Eqs. (A.3), are introduced in the continuity equation (3), leading to a diffusive-like, second order, partial differential equation (Defina, 2003). The continuity equation (3) is solved through a standard finite element Galerkin method, to yield a symmetric, positive-definite linear system with unknown the nodal free-surface elevations h. Finally, flow rates q_x and q_y are computed by back substitution of h into Eqs. A.3.

References

Abily, M., Bertrand, N., Delestre, O., Gourbesville, P., Duluc, C.M., 2016. Spatial global sensitivity analysis of high resolution classified topographic data use in 2D urban flood modelling. Environ. Modell. Softw. 77, 183–195. doi:10.1016/j.envsoft.2015.12.002.

Arrault, A., Finaud-Guyot, P., Archambeau, P., Bruwier, M., Erpicum, S., Pirotton, M., Dewals, B., 2016. Hydrodynamics of long-duration urban floods: experiments and numerical modelling. Nat. Hazard. Earth Sys. Sci. 16, 1413–1429. doi:10.5194/nhess-16-1413-2016.

Benkhaldoun, F., Elmahi, I., Moumna, A., Seaid, M., 2016. A non-homogeneous Riemann solver for shallow water equations in porous media. Appl. Anal. 95, 2181–2202. doi:10.1080/00036811.2015.1067304.

Blöschl, G., Hall, J., Parajka, J., Perdigão, R.A.P., Merz, B., Arheimer, B., Aronica, G.T., Bilibashi, A., Bonacci, O., Borga, M., Čanjevac, I., Castellarin, A., Chirico, G.B., Claps, P., Fiala, K., Frolova, N., Gorbachova, L., Gül, A., Hannaford, J., Harrigan, S., Kireeva, M., Kiss, A., Kjeldsen, T.R., Kohnová, S., Koskela, J.J., Ledvinka, O., Macdonald, N., Mavrova-Guirguinova, M., Mediero, L., Merz, R., Molnar, P., Montanari, A., Murphy, C., Osuch, M., Ovcharuk, V., Radevski, I., Rogger, M., Salinas, J.L., Sauquet, E., Šraj, M., Szolgay, J., Viglione, A., Volpi, E., Wilson, D., Zaimi, K., Živković, N., 2017. Changing climate shifts timing of European floods. Science 357, 588–590. doi:10.1126/science.aan2506.

Bruwier, M., Archambeau, P., Erpicum, S., Pirotton, M., Dewals, B., 2017. Shallow-water models with anisotropic porosity and merging for flood modelling on Cartesian grids. J. Hydrol. 554, 693–709. doi:10.1016/j.jhydrol.2017.09.051.

Bruwier, M., Mustafa, A., Aliaga, D.G., Archambeau, P., Erpicum, S., Nishida, G., Zhang, X., Pirotton, M., Teller, J., Dewals, B., 2018. Influence of urban pattern on inundation flow in floodplains of lowland rivers. Sci. Total Environ. 622–623, 446–458. doi:10.1016/j.scitotenv.2017.11.325.

Casulli, V., 2009. A high-resolution wetting and drying algorithm for free-surface hydrodynamics. Int. J. Numer. Meth. Fl. 60, 391–408. doi:10.1002/fld.1896.

Casulli, V., 2015. A conservative semi-implicit method for coupled surface-subsurface flows in regional scale. Int. J. Numer. Meth. Fl. 79, 199–214. doi:10.1002/fld.4047.

Casulli, V., Zanolli, P., 2012. Iterative solutions of mildly nonlinear systems. J. Comput. Appl. Math. 236, 3937–3947. doi:10.1016/j.cam.2012.02.042.

Cea, L., Vázquez-Cendón, M.E., 2010. Unstructured finite volume discretization of two-dimensional depth-averaged shallow water equations with porosity. Int. J. Numer. Meth. Fl. 62, 903–930. doi:10.1002/fld.2107.

Ceola, S., Laio, F., Montanari, A., 2014. Satellite nighttime lights reveal increasing human exposure to floods worldwide. Geophys. Res. Lett. 41, 7184–7190. doi:10.1002/2014GL061859.

Chen, A.S., Evans, B., Djordjević, S., Savić, D.A., 2012a. A coarse-grid approach to representing building blockage effects in 2D urban flood modelling. J. Hydrol. 426-427, 1–16. doi:10.1016/j.jhydrol.2012.01.007.

Chen, A.S., Evans, B., Djordjević, S., Savić, D.A., 2012b. Multi-layered coarse grid modelling in 2D urban flood simulations. J. Hydrol. 470-471, 1–11. doi:10.1016/j.jhydrol.2012.06.022.

Cook, A., Merwade, V., 2009. Effect of topographic data, geometric configuration and modeling approach on flood inundation mapping. J. Hydrol. 377, 131–142. doi:10.1016/j.jhydrol.2009.08.015.

Costabile, C., Costanzo, C., Macchione, F., 2017. Performances and limitations of the diffusive approximation of the 2-d shallow water equations for flood simulation in urban and rural areas. Applied Numerical Mathematics 116, 141–156. doi:10.1016/j.apnum.2016.07.003.

D'Alpaos, L., Defina, A., 2007. Mathematical modeling of tidal hydrodynamics in shallow lagoons: A review of open issues and applications to the Venice Lagoon. Comput. Geosci. 33, 476–496. doi:10.1016/j.cageo.2006.07.009.

Dankers, R., Feyen, L., 2008. Climate change impact on flood hazard in Europe: An assessment based on high-resolution climate simulations. J. Geophys. Res. Atmos. 113, D19105. doi:10.1029/2007JD009719.

Defina, A., 2000. Two dimensional shallow flow equations for partially dry areas. Water Resour. Res. 36, 3251–3264. doi:10.1029/2000WR900167.

Defina, A., 2003. Numerical experiments on bar growth. Water Resour. Res. 39(4), ESG2 1–ESG2 12. doi:10.1029/2002WR001455.

Defina, A., D'Alpaos, L., Matticchio, B., 1994. A new set of equations for very shallow water and partially dry areas suitable to 2D numerical models., in: Molinaro, P., Natale, L. (Eds.), Modelling Flood Propagation Over Initially Dry Areas.. American Society of Civil Engineers, New York, pp. 72–81.

Defina, A., Susin, F.M., Viero, D.P., 2008a. Bed friction effects on the stability of a stationary hydraulic jump in a rectangular upward sloping channel. Phys. Fluids 20, 036601. doi:10.1063/1.2841622.

Defina, A., Susin, F.M., Viero, D.P., 2008b. Numerical study of the Guderley and Vasilev reflections in steady two-dimensional shallow water flow. Phys. Fluids 20, 097102. doi:10.1063/1.2972936.

Defina, A., Viero, D.P., 2010. Open channel flow through a linear contraction. Phys. Fluids 22, 036602. doi:10.1063/1.3370334.

Doocy, S., Daniels, A., Murray, S., Kirsch, T.D., 2013. The human impact of floods: a historical review of events 1980-2009 and systematic literature review. PLoS Currents: Disasters doi:10.1371/currents.dis.f4deb457904936b07c09daa98ee8171a.

Dottori, F., Di Baldassarre, G., Todini, E., 2013. Detailed data is welcome, but with a pinch of salt: Accuracy, precision, and uncertainty in flood inundation modeling. Water Resour. Res. 49, 6079–6085. doi:10.1002/wrcr.20406.

Dottori, F., Todini, E., 2013. Testing a simple 2D hydraulic model in an urban flood experiment. Hydrol. Process. 27, 1301–1320. doi:10.1002/hyp.9370.

Douben, K.J., 2006. Characteristics of river floods and flooding: a global overview, 1985–2003. Irrig. Drain. 55, S9–S21. doi:10.1002/ird.239.

El Kadi Abderrezzak, K., Lewicki, L., Paquier, A., Rivière, N., Travin, G., 2011. Division of critical flow at three-branch open-channel intersection. J. Hydraul. Res. 49, 231–238. doi:10.1080/00221686.2011.558174.

El Kadi Abderrezzak, K., Paquier, A., Mignot, E., 2009. Modelling flash flood propagation in urban areas using a two-dimensional numerical model. Nat. Hazards 50, 433–460. doi:10.1007/s11069-008-9300-0.

Ferrari, A., Vacondio, R., Dazzi, S., Mignosa, P., 2017. A 1D–2D Shallow Water Equations solver for discontinuous porosity field based on a Generalized Riemann Problem. Adv. Water Resour. 107, 233–249. doi:10.1016/j.advwatres.2017.06.023.

Ferrari, A., Viero, D.P., Vacondio, R., Defina, A., Mignosa, P., 2019. Flood inundation modeling in urbanized areas: a mesh-independent porosity approach with anisotropic friction. Adv. Water Resour., under revision.

Finaud-Guyot, P., Delenne, C., Lhomme, J., Guinot, V., Llovel, C., 2010. An approximate-state Riemann solver for the two-dimensional shallow water equations with porosity. Int. J. Numer. Meth. Fl. 62, 1299–1331. doi:10.1002/fld.2066.

Giraldo, F.X., 2000. The Lagrange-Galerkin method for the two-dimensional shallow water equations on adaptive grids. Int. J. Numer. Meth. Fl. 33, 789–832. doi:10.1016/S0898-1221(03)80010-X.

Graebel, W.P., 2007. Advanced Fluid Mechanics. Academic Press, London.
Guinot, V., 2012. Multiple porosity shallow water models for macroscopic modelling of urban floods. Adv. Water Resour. 37, 40–72. doi:10.1016/j.advwatres.2011.11.002.
Guinot, V., 2017a. Consistency and bicharacteristic analysis of integral porosity shallow water models. Explaining model oversensitivity to mesh design. Adv. Water Resour. 107, 43–55. doi:10.1016/j.advwatres.2017.06.008.
Guinot, V., 2017b. A critical assessment of flux and source term closures in shallow water models with porosity for urban flood simulations. Adv. Water Resour. 109, 133–157. doi:10.1016/j.advwatres.2017.09.002.
Guinot, V., Delenne, C., Rousseau, A., Boutron, O., 2018. Flux closures and source term models for shallow water models with depth-dependent integral porosity. Adv. Water Resour. 122, 1–26. doi:10.1016/j.advwatres.2018.09.014.
Guinot, V., Sanders, B.F., Schubert, J.E., 2017. Dual integral porosity shallow water model for urban flood modelling. Adv. Water Resour. 103, 16–31. doi:10.1016/j.advwatres.2017.02.009.
Guinot, V., Soares-Frazão, S., 2006. Flux and source term discretization in two-dimensional shallow water models with porosity on unstructured grids. Int. J. Numer. Meth. Fl. 50, 309–345. doi:10.1002/fld.1059.
Hodges, B.R., 2015. Representing hydrodynamically important blocking features in coastal or riverine lidar topography. Nat. Hazard. Earth Sys. Sci. 15, 1011–1023. doi:10.5194/nhess-15-1011-2015.
Hunter, N.M., Bates, P.D., Neelz, S., Pender, G., Villanueva, I., Wright, N.G., Liang, D., Falconer, R.A., Lin, B., Waller, S., Crossley, A.J., Mason, D.C., 2008. Benchmarking 2D hydraulic models for urban flooding. Proceedings of the Institution of Civil Engineers - Water Management 161, 13–30. doi:10.1680/wama.2008.161.1.13.
Kim, B., Sanders, B., Famiglietti, J.S., Guinot, V., 2015. Urban flood modeling with porous shallow-water equations: A case study of model errors in the presence of anisotropic porosity. J. Hydrol. 523, 680–692. doi:10.1016/j.jhydrol.2015.01.059.
Kong, J., Xin, P., Song, Z.Y., Li, L., 2010. A new model for coupling surface and subsurface water flows: With an application to a lagoon. J. Hydrol. 390, 116–120. doi:10.1016/j.jhydrol.2010.06.028.
Kramer, S.C., Stelling, G.S., 2008. A conservative unstructured scheme for rapidly varied flows. Int. J. Numer. Meth. Fl. 58, 183–212. doi:10.1002/fld.1722.
Liang, D., Falconer, R.A., Lin, B., 2007. Coupling surface and subsurface flows in a depth averaged flood wave model. J. Hydrol. 337, 147–158. doi:10.1016/j.jhydrol.2007.01.045.
Luo, H., Fytanidis, D.K., Schmidt, A.R., García, M.H., 2018. Comparative 1D and 3D numerical investigation of open-channel junction flows and energy losses. Adv. Water Resour. 117, 120–139. doi:10.1016/j.advwatres.2018.05.012.
McMillan, H.K., Brasington, J., 2007. Reduced complexity strategies for modelling urban floodplain inundation. Geomorphology 90, 226–243. doi:10.1016/j.geomorph.2006.10.031.
Meesuk, V., Vojinovic, Z., Mynett, A.E., Abdullah, A.F., 2015. Urban flood modelling combining top-view LiDAR data with ground-view SfM observations. Adv. Water Resour. 75, 105–117. doi:10.1016/j.advwatres.2014.11.008.
Mignot, E., Paquier, A., Haider, S., 2006. Modeling floods in dense urban areas using 2D shallow water equations. J. Hydrol. 327, 186–199.
Mignot, E., Paquier, A., Rivière, N., 2008. Experimental and numerical modeling of symmetrical four-branch supercritical. J. Hydraul. Res. 46, 723–738. doi:10.1080/00221686.2008.9521918.
Mignot, E., Zeng, C., Dominguez, G., Li, C.W., Riviére, N., Bazin, P.H., 2013. Impact of topographic obstacles on the discharge distribution in open-channel bifurcations. J. Hydrol. 494, 10–19. doi:10.1016/j.jhydrol.2013.04.023.
Muis, S., Güneralp, B., Jongman, B., Aerts, J.C.J.H., Ward, P.J., 2015. Flood risk and adaptation strategies under climate change and urban expansion: A probabilistic analysis using global data. Sci. Total Environ. 538, 445–457. doi:10.1016/j.scitotenv.2015.08.068.
Neal, J.C., Bates, P.D., Fewtrell, T.J., Hunter, N.M., Wilson, M.D., Horritt, M.S., 2009. Distributed whole city water level measurements from the Carlisle 2005 urban flood event and comparison with hydraulic model simulations. J. Hydrol. 368, 42–55. doi:10.1016/j.jhydrol.2009.01.026.
Neelz, S., Pender, G., 2007. Sub-grid scale parameterisation of 2D hydrodynamic models of inundation in the urban area. Acta Geophysica 55, 65–72. doi:10.2478/s11600-006-0039-2.
Noh, S.J., Lee, J.H., Lee, S., Kawaike, K., Seo, D.J., 2018. Hyper-resolution 1D-2D urban flood modelling using LiDAR data and hybrid parallelization. Environ. Modell. Softw. 103, 131–145. doi:10.1016/j.envsoft.2018.02.008.
Özgen, I., Liang, D., Hinkelmann, R., 2015. Shallow water equations with depth-dependent anisotropic porosity for subgrid-scale topography. Appl. Math. Model. 40(17–18), 7447–7473. doi:10.1016/j.apm.2015.12.012.
Özgen, I., Zhao, J., Liang, D., Hinkelmann, R., 2016. Urban flood modeling using shallow water equations with depth-dependent anisotropic porosity. J. Hydrol. 541, 1165–1184. doi:10.1016/j.jhydrol.2016.08.025.
Perot, B., 2000. Conservation properties of unstructured staggered mesh schemes. J. Comput. Phys. 159, 58–89. doi:10.1006/jcph.2000.6424.
Petaccia, G., Soares-Frazão, S., Savi, F., Natale, L., Zech, Y., 2010. Simplified versus detailed two-dimensional approaches to transient flow modeling in urban areas. J. Hydraul. Eng. 136, 262–266. doi:10.1061/(ASCE)HY.1943-7900.0000154.
Rivière, N., Travin, G., Perkins, R.J., 2011. Subcritical open channel flows in four branch intersections. Water Resour. Res. 47. doi:10.1029/2011WR010504.
Rivière, N., Travin, G., Perkins, R.J., 2014. Transcritical flows in three and four branch open-channel intersections. J. Hydraul. Eng. 140, 04014003. doi:10.1061/(ASCE)HY.1943-7900.0000835.
Sanders, B.F., Schubert, J.E., Gallegos, H.A., 2008. Integral formulation of shallow-water equations with anisotropic porosity for urban flood modeling. J. Hydrol. 362, 19–38. doi:10.1016/j.jhydrol.2008.08.009.
Schubert, J.E., Sanders, B.F., 2012. Building treatments for urban flood inundation models and implications for predictive skill and modeling efficiency. Adv. Water Resour. 41, 49–64. doi:10.1016/j.advwatres.2012.02.012.
Soares-Frazao, S., Lhomme, J., Guinot, V., Zech, Y., 2008. Two-dimensional shallow-water model with porosity for urban flood modelling. J. Hydraul. Res. 46, 45–64. doi:10.1080/00221686.2008.9521842.
Stansby, P.K., 2003. A mixing length model for shallow turbulent wakes. J. Fluid Mech. 495, 369–384. doi:10.1017/S0022112003006384.
Syvitski, J.P.M., Kettner, A.J., Overeem, I., Hutton, E.W.H., Hannon, M.T., Brakenridge, G.R., Day, J., Vörösmarty, C., Saito, Y., Giosan, L., Nicholls, R.J., 2009. Sinking deltas due to human activities. Nat. Geosci. 2, 681–686. doi:10.1038/ngeo629.

Teng, J., Jakeman, A.J., Vaze, J., Croke, B.F., Dutta, D., Kim, S., 2017. Flood inundation modelling: A review of methods, recent advances and uncertainty analysis. Environ. Modell. Softw. 90, 201–216. doi:10.1016/j.envsoft.2017.01.006.

Uittenbogaard, R.R., van Vossen, B., 2004. Subgrid-scale model for quasi-2D turbulence in shallow water., in: Uijttewaal, W.S.J., Jirka, G.H. (Eds.), Shallow Flows. Taylor & Francis Group, London, pp. 575–582. doi:10.1201/9780203027325.ch72.

United Nations, 2015. World Population Prospects: The 2015 Revision, Key Findings and Advance Tables. Technical Report. United Nations, Department of Economic and Social Affairs, Population Division. Working Paper No. ESA/P/WP.241.

Velickovic, M., Zech, Y., Soares-Frazão, S., 2017. Steady-flow experiments in urban areas and anisotropic porosity model. J. Hydraul. Res. 55, 85–100. doi:10.1080/00221686.2016.1238013.

Viero, D.P., D'Alpaos, A., Carniello, L., Defina, A., 2013a. Mathematical modeling of flooding due to river bank failure. Adv. Water Resour. 59, 82–94. doi:10.1016/j.advwatres.2013.05.011.

Viero, D.P., Defina, A., 2016. Water age, exposure time, and local flushing time in semi-enclosed, tidal basins with negligible freshwater inflow. J. Marine Syst. 156, 16–29. doi:10.1016/j.jmarsys.2015.11.006.

Viero, D.P., Peruzzo, P., Carniello, L., Defina, A., 2014. Integrated mathematical modeling of hydrological and hydrodynamic response to rainfall events in rural lowland catchments. Water Resour. Res. 50, 5941–5957. doi:10.1002/2013WR014293.

Viero, D.P., Peruzzo, P., Defina, A., 2017. Positive surge propagation in sloping channels. Water 9, 518. doi:10.3390/w9070518.

Viero, D.P., Roder, G., Matticchio, B., Defina, A., Tarolli, P., 2019. Floods, landscape modifications and population dynamics in anthropogenic coastal lowlands: The Polesine (northern Italy) case study. Sci. Total Environ. 651, 1435–1450. doi:10.1016/j.scitotenv.2018.09.121.

Viero, D.P., Susin, F.M., Defina, A., 2013b. A note on weak shock wave reflection. Shock Waves 23, 505–511. doi:10.1007/s00193-013-0452-9.

Viero, D.P., Valipour, M., 2017. Modeling anisotropy in free-surface overland and shallow inundation flows. Adv. Water Resour. 104, 1–14. doi:10.1016/j.advwatres.2017.03.007.

Walters, R.A., Casulli, V., 1998. A robust, finite element model for hydrostatic surface water flows. Commun. Numer. Meth. Engng. 14, 931–940. doi:10.1002/(SICI)1099-0887(1998100)14:10<931::AID-CNM199>3.0.CO;2-X.

Wang, Y., Chen, A.S., Fu, G., Djordjević, S., Zhang, C., Savić, D.A., 2018. An integrated framework for high-resolution urban flood modelling considering multiple information sources and urban features. Environ. Modell. Softw. 5, 644–656. doi:10.1016/j.envsoft.2018.06.010.

Weber, L.J., Schumate, E.D., Mawer, N., 2001. Experiments on flow at a 90° open-channel junction. J. Hydraul. Eng. 127, 340–350. doi:10.1061/(ASCE)0733-9429(2001)127:5(340).

Whitfield, P., 2012. Floods in future climates: a review. J. Flood Risk Manag. 5, 336–365. doi:10.1111/j.1753-318X.2012.01150.x.

Yu, D., Lane, S.N., 2006. Urban fluvial flood modelling using a two-dimensional diffusion-wave treatment. Part 2: development of a sub-grid-scale treatment. Hydrol. Process. 20, 1567–1583. doi:10.1002/hyp.5936.

Yu, D., Lane, S.N., 2011. Interactions between subgrid-scale resolution, feature representation and grid-scale resolution in flood inundation modelling. Hydrol. Process. 25, 36–53. doi:10.1002/hyp.7813.

Yuan, D., Lin, B., Falconer, R.A., 2008. Simulating moving boundary using a linked groundwater and surface water flow model. J. Hydrol. 349, 524–535. doi:10.1016/j.jhydrol.2007.11.028.